Numerical Simulation of Reactive Pulsing Flow for the Catalytic Wet Oxidation in TBR Using a VOF Technique

Rodrigo J. G. Lopes, Vera S. L. de Sousa, and Rosa M. Quinta-Ferreira
Research Centre for Chemical Processes and Forest Products, Dept. of Chemical Engineering, Group on Environmental, Reaction and Separation Engineering (GERSE), University of Coimbra, Rua Sílvio Lima, Polo II–Pinhal de Marrocos, 3030-790 Coimbra, Portugal

DOI 10.1002/aic.12585
Published online March 14, 2011 in Wiley Online Library (wileyonlinelibrary.com).

Guided by the intrinsic advantages of the dynamic nature of mass/heat transfer fluctuations in pulsing flow, here we performed volume-of-fluid (VOF) numerical simulations to evaluate how liquid flow modulations can improve the detoxification of liquid effluents by catalytic wet oxidation. First, prominent numerical parameters were optimized in terms of mesh aperture and time step. Second, the effect of oxidation temperature and the influence of gas and liquid flow rates have been investigated comparatively under different flow regimes. The VOF computations have correctly handled the experimental observations both in terms of the axial conversion and temperature. The increase of oxidation temperature was found to move the trickling and pulsing intersection point on the conversion toward the top of the trickle bed. Finally, in comparison with trickling flow regimes, these computed and experimental findings revealed a considerable improvement on the detoxification of organic matter highlighting the benefits of process intensification covered by the periodic liquid flow modulations. © 2011 American Institute of Chemical Engineers *AIChE J,* 58: 493–504, 2012
Keywords: volume-of-fluid, trickle-bed reactor, pulsing flow, catalytic wet oxidation, numerical simulation

Introduction

Pulsing flow in trickle-bed reactors (TBRs) has been claimed to promote the averaged heat and mass transfer rates, thereby enhancing the overall conversion and productivity. The gas–liquid cocurrent flow in these packed bed reactors found common applications in the petrochemical industries where hydrotreating reactions of the various petroleum fractions play a major role.[1] More recently, the unprecedented number of publications devoted to biochemical processes and advanced oxidation processes have envisaged TBRs for the purification of wastewaters and gases polluted with toxic organic compounds using a bed of immobilized bacteria or chemical catalyst, respectively.[2] As trickle beds are governed by different hydrodynamic states, the literature has primarily reported on trickle and pulse flow regimes in view of the fact that these contacting patterns are conventionally encountered in commercial-scale trickle beds. Our case study follows up the long-standing interest on the environmental applications of trickle beds in catalytic wet oxidation to realize theoretically and experimentally the advantages of the convective nature of liquid disturbances that grow into pulses in TBRs.[3,4]

As long as pulsing flow regime has been used to improve the hydrogenation reactions in the field of petrochemical industry, there exists a considerable room in environmental

Correspondence concerning this article should be addressed to R. J. G. Lopes at rodrigo@eq.uc.pt.

applications to improve the understanding on the nature and the characteristics of the hydrodynamics in those flow regimes and the transition between them. In an attempt to realize such a task, precise tools are required for the identification of the flow pattern and the reaction behavior. Important emphasis is being put nowadays on advanced computational fluid dynamics (CFD) codes to deal with an accurate prediction of the trickle-to-pulse flow transition, which is a key feature of major importance in the characterization of flow pattern apart from the quantification of phase holdups, two-phase frictional pressure drop, and mass fluxes. Here, we focus on the development of a CFD framework embedded with a volume-of-fluid (VOF) model to evaluate how catalytic wet oxidation can be promoted when the trickle flow regime evolves to the pulse flow regime. The pulsing hydrodynamic regime is attained at severe flow conditions, where sharp, structured, and traveling disturbances of high-liquid holdup substitutes the low interaction regime achieved under trickling flow conditions. Being aware that pulsing flows affect the heat and mass transfer rates, and thus reaction rates, hence it is necessary to grasp how superior the detoxification of phenol-like pollutants can be improved by catalytic wet air oxidation.

Previous Work

More than two decades have now passed since the publication of a cross-flow model for pulsing flow in a trickle bed of large cross-section by Sundaresan.[5] The author has assumed the macroscopic gas flow around the pulses to be irrotational and the pulses to contain only liquid to derive the model equations. The irrotational flow model was found to underestimate the pulse velocity for realistic pulse shapes, which has been explained by the drag exerted by the trickling region on the pulses. This fact has been overtaken by using a semiempirical approach. Grosser et al.[6] have discriminated the onset of pulsing in two-phase cocurrent downflow through a packed bed. A simple macroscopic model for the two-phase flow was analyzed to examine whether this regime transition should be viewed as the loss of stability of a steady state or the loss of existence of any solution for the steady-state equations of motion. It was found that the former fact appeared to be a more reasonable interpretation and an explicit algebraic criterion for the onset of pulsing was presented. Dankworth et al.[7] investigated the dynamics of pulsing flow in trickle beds by means of a macroscopic model of two-phase flow based on the volume-averaged equations of motion for the gas and liquid phases. Aiming to understand the onset and evolution of fully developed pulsing flow in trickle beds, the authors have taken solutions in the form of waves traveling at constant speed to obtain periodic solutions. The numerical results have been found to predict the properties of one-dimensional pulses and allowed to identify the hysteresis in the trickling-pulsing transition. Wilhite et al.[8] carried out an experimental study following the theoretical work to demonstrate how pulsing flow regime can enhance three-phase packed bed reactor performance. It has been claimed that the reaction yield is higher in pulsing flow than in trickling flow by evaluating systematically the effects of process variables such as temperature, feed flow rates, and reactant concentration on reaction behavior.

An advanced experimental technique has been used by Anadon et al.[9] to investigate the mechanism of the trickle-to-pulse flow transition in fixed-bed reactors. The formation of local instabilities, identified as isolated pulsing events using ultrafast magnetic resonance imaging, in the gas–liquid distribution within a TBR was shown to be central to the origin of the hydrodynamic transition from trickle-to-pulsing flow. The criterion for the identification of the transition point was defined to be the liquid velocity at which the maximum number of isolated pulses occurs at a given gas velocity and they have critically compared the experimental data with the predictions of existing correlations and theoretical models.

From a theoretical perspective, mathematical frameworks based on multiphase CFD models have been published concerning one-dimensional and multidimensional flow solvers on the prediction of global hydrodynamic parameters. Attou and Ferschneider[10] presented simulations for the first rank of solvers without accounting for radial variation in bed porosity. Conversely, Jiang et al.[11] have developed a two-dimensional CFD model able to capture some of the key features of hydrodynamics of trickle beds, whereas Iliuta et al.[12] and Souadnia and Latafi[13] have used the CFD model for predicting hydrodynamics characteristics over a wide range of operating parameters. Gunjal et al.[14] have used a similar CFD model for studying liquid phase mixing and liquid distribution. However, both of these studies were restricted to trickle flow regime. None of the CFD models published so far was used to simulate spray or pulse regimes or even the multiphase reacting flows.

This work extends our initial efforts at conducting CFD simulations and experimental validation to verify the theoretical predictions on the mineralization of organic matter at different liquid flow modulations. It would not be sufficient to conduct one set of experiments at flow conditions without querying the influence of gas and liquid flow rates, because these operating parameters have a priori a considerable effect on the reaction result. Likewise, different oxidation temperatures would be adequate to demonstrate how pulsing flows enhance the detoxification efficiency. Therefore, a VOF-based model coupled with transport processes such as heat- and mass-transfer rates is firstly developed accounting for the dependency of flow regimes and extent of interaction among gas, liquid, and solid phases. The aim of this work is to evaluate the catalytic wet oxidation performance of liquid flow alternating cyclic operation and comparing it with similar gas and liquid superficial velocities that are kept within the range of trickle flow regime.

The remainder of this article is organized as follows: the multiphase flow governing equations are detailed with the computational methodology used in the simulation procedure followed by the simulation setup and the relevant boundary conditions. The succeeding section describes the experimental procedure. After optimized, the numerical solution parameters, results, and discussions are presented encompassing qualitative and quantitative comparisons of computed and experimental TOC concentration and temperature profiles. The morphological features of liquid holdup pulsation under cyclic operation are correlated with the concentration and thermal profiles. Finally, diagrammatic representations of interstitial flow are briefly analyzed by three-dimensional computational mappings of computed concentration results.

CFD Methodology

VOF equations

The CFD model equations were implemented in commercial software FLUENT and only the main conservation equations are presented here. The VOF method was used to compute velocity field, liquid volume fraction distributions, and the total organic carbon concentration that was used to quantify the mineralization degree of liquid pollutants. The multiphase flow is assumed to be vertical downward and incompressible, with the mathematical description for the flow of a viscous fluid through a three-dimensional catalytic bed based on the Navier–Stokes equations for momentum and mass conservation. The variable fields are shared by both phases and correspond to volume-averaged values knowing the volume fraction, α_q, of each phase, q, in the entire computational domain. The volume fraction equation for the phase q is given by:

$$\frac{\partial}{\partial t}\left(\alpha_q \rho_q\right) + \nabla \cdot \left(\alpha_q \rho_q \mathrm{U}_q\right) = 0 \quad \text{with } q = \mathrm{g} \text{ or } \mathrm{l} \tag{1}$$

where g and l denote, respectively, the gas and liquid phases, t, being the time, and through the resolution of the momentum equation shared by the two considered fluids:

$$\frac{\partial}{\partial t}\left(\alpha_q \rho_q \mathrm{U}_q\right) + \nabla \cdot \left(\alpha_q \rho_q \mathrm{U}_q \mathrm{U}_q\right) = -\alpha_q \nabla p + \alpha_q \rho_q \mathbf{g} + \nabla \cdot \alpha_q \left(\overline{\overline{\tau_q}} + \overline{\overline{\tau_{t,q}}}\right) + I_q \quad \text{with } q = \mathrm{g} \text{ or } \mathrm{l} \tag{2}$$

where p, $\mathbf{g}$, and the physical properties (density, ρ; and viscosity, μ) being determined by volume-weighted averages. $\mathbf{I}_q$ is the interphase momentum exchange term similarly derived by Lopes et al.,[15] and $\overline{\overline{\tau_q}}$ and $\overline{\overline{\tau_{t,q}}}$ are, respectively, the viscous stress tensor and the turbulent stress tensor, defined as follows:

$$\overline{\overline{\tau_q}} = \mu_q \left(\nabla \mathrm{U}_q + \nabla \mathrm{U}_q^t\right) + \left(\lambda_q - \frac{2}{3}\mu_q\right) \nabla \mathrm{U}_q \bar{\bar{I}} \tag{3}$$

and

$$\overline{\overline{\tau_{t,q}}} = \mu_{t,q} \left(\nabla \mathrm{U}_q + \nabla \mathrm{U}_q^t\right) - \frac{2}{3}\left(k_q + \mu_{t,q} \nabla \mathrm{U}_q\right) \bar{\bar{I}} \tag{4}$$

We have used the free surface model to compute the surface tension and wall adhesion as originally presented by Brackbill et al.[16] To deal with the changeover of the gas continuous flow regime to the pulsing flow regime, two hydrodynamic models were developed for the comparison between the transition lines obtained experimentally with the mathematical criteria available in the literature that are the models of Grosser et al.[6] and Attou and Ferschneider.[10] The criterion was based on the linear stability analysis of the equations describing the multiphase flow in trickle beds. In the present work, we have used the polynomial form of the criterion presented by Attou and Ferschneider[10] coupled with the model originally investigated by Lopes and Quinta-Ferreira.[17] Continuity and momentum Eqs. 1 and 2 are functionally equivalent to the set of equations used by Grosser et al.,[6] which were implemented in C language in the CFD framework for the trickle-to-pulse transition. Using this methodology, the analysis of Grosser et al.[6] and Attou and Ferschneider[10] yielded the following expressions for F_i coefficients, and the stability condition is established such that the real part of the attenuation factor or the pulsation of the harmonic perturbation (s) is less or equal to zero, which gives Eqs. 5 and 6:

$$\Omega \equiv F_1 F_5^2 + 2F_2 F_3 F_5 + F_2^2 F_4 \leq 0 \tag{5}$$

$$F_1 s^2 + (F_2 + 2\mathrm{j}\omega F_3)s - \left(\omega^2 F_4 + \mathrm{j}\omega F_5\right) = 0 \tag{6}$$

Equations of this type include s, which is the complex frequency, ω is the real wave number in the vertical flow direction, and j yields the neutral stability condition where the coefficients F_i are given by:

$$F_1 = \frac{\rho_G}{\alpha_G} + \frac{\rho_L}{(1-\alpha_G)} \tag{7}$$

$$F_2 = -\frac{\lambda_{G,u_G}}{\alpha_G^2} - \frac{\lambda_{L,u_L} + \pi_{L,u_L}}{(1-\alpha_G)^2} + \frac{\lambda_{L,u_G} + \lambda_{G,u_L}}{\alpha_G(1-\alpha_G)} \tag{8}$$

$$F_3 = \frac{\rho_G u_G}{\alpha_G} + \frac{\rho_L u_L}{(1-\alpha_G)} \tag{9}$$

$$F_4 = \frac{\rho_G u_G^2}{\alpha_G} + \frac{\rho_L u_L^2}{(1-\alpha_G)} - \left[\frac{\partial}{\partial \alpha_G}(p_G - p_L)\right] \tag{10}$$

$$F_5 = \frac{f_{\mathrm{int},L} + f_{w,L}}{(1-\alpha_G)^2} + \frac{f_{\mathrm{int},G}}{\alpha_G^2} + u_G\left(\frac{\lambda_{G,u_G}}{\alpha_G^2} - \frac{\lambda_{L,u_G}}{\alpha_G(1-\alpha_G)}\right) + u_L\left(\frac{\lambda_{L,u_L} + \pi_{L,u_L}}{(1-\alpha_G)^2} - \frac{\lambda_{G,u_L}}{\alpha_G(1-\alpha_G)}\right) + \frac{\lambda_{L,\alpha_G}}{(1-\alpha_G)} - \frac{\lambda_{G,\alpha_G}}{\alpha_G} \tag{11}$$

and λ_{q,u_q} and π_{L,u_L} are derivative quantities defined, respectively, by Eq. 12.

$$\lambda_{q,u_q} = \nabla f_{\mathrm{int},q}; \quad \pi_{L,u_L} = \frac{\partial f_{w,L}}{\partial u_L} \tag{12}$$

$f_{\mathrm{int},q}$ includes two components for the resultant of the forces exerted on the gas phase due to the slip motion between the two fluids and the force by which the gas pushes the liquid film against the catalyst particles due to the tortuous pattern and the successive cross-sectional area changes of the interstitial flow path. In the case of the liquid phase, $f_{\mathrm{int},q}$ involves the drag force exerted on the liquid film due to the shear stress at the vicinity of the packing surface and the gas–liquid drag force resulting from the slip between the two fluids. Based on the Kozeny–Carman's formulation, $f_{\mathrm{int},q}$ is given by the following closure Eqs. 13 and 14:

$$f_{\mathrm{int},G} = -\alpha_G(A_{GL}\alpha_G\mu_G(j_r + j_G) + B_{GL}\alpha_G\rho_G(j_r|j_r| + j_G|j_G|)) \tag{13}$$

$$f_{\mathrm{int},L} = \alpha_G(A_{GL}\alpha_G\mu_G j_r + B_{GL}\alpha_G\rho_G j_r|j_r|) - (A_{LS}\alpha_G\mu_L j_L + B_{LS}\alpha_G\rho_L j_L|j_L|) \tag{14}$$

where $j_K = \varepsilon\alpha_q u_q$ is the superficial velocity of q-phase, and $j_r = j_G - (\alpha_G/(1-\alpha_G))j_L$ is a reference superficial velocity for the gas–velocity slip motion. A_{qp} and B_{qp} are the viscous and

inertial terms of Kozeny–Carman's equation. $f_{w,L}$ accounts for the wall friction force and is determined from the formulation of the empty pipe flows: $f_{w,L} = -4\tau_{w,L}/\alpha D$, where $\tau_{w,L}$ is the wall shear stress, and D is the reactor diameter.

Species continuity and energy equations

The predicted flow field including velocities and volume fractions of both phases was further used for solving species transport equations for simulating the catalytic wet air oxidation of a model phenolic solution in the TBR. These equations are expressed in the mass balance equation for any species, i:

$$\frac{\partial \alpha_q \rho_q C_{q,i}}{\partial t} + \nabla \cdot \left(\alpha_q \rho_q u_q C_{q,i}\right) = \nabla \cdot \left(\alpha_q \rho_q D_{q,i} \nabla C_{q,i}\right) + \nabla \cdot \alpha_q \rho_q S_{q,i} \quad (15)$$

where, $C_{q,i}$ is the concentration of species i in the qth phase (gas or liquid), ρ_q and α_q are the density and volume fractions of the qth phase. $S_{q,i}$ is the source for species i in phase q. Volume-averaged properties of fluids were used for calculating the flux across the control cell. Two-film theory was used for accounting mass transfer. The resistance in gas–liquid film was considered as the rate-limiting resistance.[2,18] Mass-transfer coefficient was computed according to the correlation developed by Satterfield et al.,[19] and heat-transfer coefficient was calculated according to the correlation developed by Boelhouwer et al.[20] as expressed by Eqs. 16 and 17, respectively.

$$Sh = 0.815\, Re^{0.822} Sc^{1/3} \quad (16)$$

$$Nu = 0.111\, Re^{0.8} Pr^{1/3} \quad (17)$$

The energy equation, also shared among the phases, is shown in Eq. 18:

$$\frac{\partial}{\partial t}(\rho E) + \nabla \cdot (\vec{v}(\rho E + p)) = \nabla \cdot (k_{\text{eff}} \nabla T) + S_h \quad (18)$$

The VOF model treats energy, E, and temperature, T, as mass-averaged variables:

$$E = \frac{\sum_{q=1}^{n} \alpha_q \rho_q E_q}{\sum_{q=1}^{n} \alpha_q \rho_q} \quad (19)$$

where E_q for each phase is based on the specific heat of that phase and the shared temperature. The properties ρ and k_{eff} (effective thermal conductivity) are shared by the phases. The source term, S_h, contains contributions from volumetric reaction heat sources, which is given by the product $\Delta H \times \rho \times r_{\text{TOC}}$. The catalytic wet air oxidation kinetic parameters for the commercial catalyst N-140 were derived for the continuous treatment following the screening work described elsewhere.[21] The right-hand side term of Eq. 15, $S_{q,i}$, includes the reaction rates in terms of the total organic carbon concentration of the lumped species A, B, and C as represented by Eq. 20.

$$\begin{aligned} -r_{\text{TOC}_\text{A}} &= -\frac{d\,C_{\text{TOC}_\text{A}}}{dt} = \left(k'_1 + k'_2\right)\, C_{\text{TOC}_\text{A}} \\ -r_{\text{TOC}_\text{B}} &= -\frac{d\,C_{\text{TOC}_\text{B}}}{dt} = k'_3\, C_{\text{TOC}_\text{B}} - k'_2\, C_{\text{TOC}_\text{A}} \end{aligned} \quad (20)$$

where first-order reactions were assumed for each mechanism step of the generalized kinetic model. The activation energies and the pre-exponential factors were calculated by using the Arrhenius plot for the N-140 kinetic studies. These values were used in the corresponding expressions of the reaction rate constants k'_1, k'_2,, and k'_3, as functions of temperature, according to Arrhenius law as described in Eq. 21.

$$\begin{aligned} k'_1 &= 452 \cdot \exp\left(-\frac{3.121 \times 10^3}{T}\right) \text{min}^{-1}; \\ k'_2 &= 28.1 \cdot \exp\left(-\frac{3.612 \times 10^3}{T}\right) \text{min}^{-1}; \\ k'_3 &= 4.32 \times 10^6 \cdot \exp\left(-\frac{9.814 \times 10^3}{T}\right) \text{min}^{-1} \end{aligned} \quad (21)$$

Simulation and experimental setup

The representative computational grid for the experimental system investigated in this work is described elsewhere.[17] It consists of a cylindrical vessel with 5-cm internal diameter and 1-m bed height packed with catalyst spherical particles 2-mm diameter. The catalytic bed is meshed in tetrahedral cells by means of the FLUENT preprocessor GAMBIT 2. The mesh quality was analyzed using the skewness criteria, and the results were optimized to be grid independent. Numerical simulations were compared previously with experimental data to validate the predicted hydrodynamic parameters pressure drop and liquid holdup.[17] The system domain is discretized by an unstructured finite volume method using the CFD solver FLUENT 6. The gas flow rate at the distributor is defined via inlet-velocity-type boundary condition with gas volume fraction charging according to the specifications made in the simulations. The governing differential equations are solved using iterative solution to the discrete form of the mathematical model using a PISO algorithm for pressure–velocity coupling with implicit formulation for unsteady integration and second-order upwind scheme discretization for spatial derivatives. The transient calculations were made for two-phase flow starting with different time steps, and the converged solution is assumed when the scaled residuals of all variables were smaller than 10^{-6}.

The TBR studies have been carried out in a pilot plant comprising a cylindrical reactor in stainless steel (SS-316) with 50 mm of internal diameter and 1.0-m length described elsewhere.[22] The reactor was placed in a temperature-controlled oven and is equipped with pressure and temperature control units and a separation and sampling system for the outlet products. Gas and liquid preheated feed were introduced at the top of the reactor. The volumetric liquid flow rate was cycled by means of an ON–OFF three-way solenoid valve to evaluate a periodically operated TBR. There was no liquid flow during the dry period, which corresponds to the ON–OFF cycling strategy. Since only a few minutes are needed to drain the bed, ON–OFF operation was considered

as square waves cycling. The liquid flow rate was set as to obtain the same productivity as in steady-state operation. The liquid velocity for steady state and during the wet cycle of periodic operation are related with the cycle split, which is the fraction of the cycle during which the liquid phase flushes the bed.

To evaluate the ON–OFF liquid flow modulation, we have designed the cyclic operation parameters either to the fractional period feed flow, which was ON and OFF, or to the reciprocal of the total period. For example, a mode of 10 s ON−10 s OFF means that liquid flows for 10 s followed by 10 s of flow interruption. The cycle frequency is $1/(10 + 10) = 0.05$ Hz. We have found that the frequency of the traveling liquid pulsations did not change along the bed and remains at the preimposed value. In addition, only computed and experimental reaction data obtained for symmetric splits with equal ON and OFF time durations are addressed in this work. Having proposed symmetric splits for liquid flow, the barycentric superficial velocity counts for half the actually imposed superficial velocity during the ON sequence. The propagation along the bed main axis of the periodic liquid pulsations was examined via total organic carbon conversions at different bed elevations.

Results and Discussion

VOF optimization of grid density and time step

First, we have assessed this process intensification technique from a numerical point of view, and how it can improve the performance of catalytic abatement of hazardous compounds in the TBR. Under pulsing flow conditions (PFCs), the process methodology encompassed by liquid flow modulation confers distinct hydrodynamic features with respect to steady-state operation. Our periodic workflow experiments can be described as a mode of process in which the system is forced to operate continuously in a transient mode. This experimental technique did not exhibit a seamless flow pattern but rather consisted of scattered loads of liquid pockets that can a priori eliminate the in situ development of bed maldistribution. A key issue relies on the achievement of grid convergence; so, to deal with the complexity of numerical simulations under PFCs, a preliminary task was accomplished to control the numerical solution accuracy by modifying the domain discretization according to size and directional constraints. The computational grid was optimized for time-dependent simulations as the application of a uniformly fine mesh size everywhere would be time-consuming /to preserve the solution accuracy.

Four levels for the coarser meshes with 2×10^5, 6×10^5, 1×10^6, and 1.4×10^6 of tetrahedral cells and four levels for the finer meshes with 1.8×10^6, 2.2×10^6, 2.6×10^6, and 3×10^6 of tetrahedral cells have been used to evaluate quantitatively the tetrahedral mesh aperture. Figure 1 displays the influence of the number of tetrahedral cells on the total organic carbon conversion profile when the catalytic oxidation of phenolic wastewaters was simulated at $G = 0.5$ kg/m^{2}s, $T = 200$°C, and $P = 30$ bar following the ON–OFF liquid flow modulation: $L = 9$ kg/m^{2}s $\rightarrow L = 3$ kg/m^{2}s $\rightarrow L = 9$ kg/m^{2}s. As can be seen form Figure 1, the increase of grid cells from 2×10^5, 6×10^5, 1×10^6, 1.4×10^6 to 1.8×10^6, 2.2×10^6, 2.6×10^6, 3×10^6 of computational

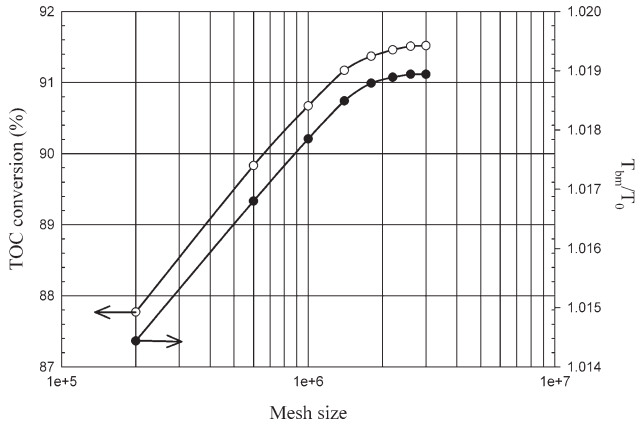

Figure 1. Comparison of CFD predictions on Total Organic Carbon conversion and normalized bulk temperature for different mesh resolutions.

$T = 200$ °C, $G = 0.5$ kg/m^{2}s, $P = 30$ bar, ON–OFF liquid flow modulation: $L = 9$ kg/m^{2}s $\rightarrow L = 3$ kg/m^{2}s $\rightarrow L = 9$ kg/m^{2}s.

nodes led to the following reaction conversions: 87.77, 89.83, 90.65, 91.19 and 91.34, 91.49, 91.51, 91.52%, respectively. The finest tetrahedral mesh with 3×10^6 cells handled agreeably better the experimental data on the total organic carbon concentration. In fact, the asymptotic solution attained when increasing the number of computational nodes from 2.4×10^6 onward allows one to infer that the finer mesh resolutions led to confident predictions on the conversion profile. This fact can be explained by the representative nature of time-dependent pulsing flow regimes. As long as the progression of moving phenomena in the complex fixed geometry of the trickle bed is known to be characterized by incomplete catalyst wetting for trickling flow regimes, additional concerns arose for the ON–OFF liquid flow simulations. To cope with these numerical issues on dealing with mesh adaptation, we increased systematically the number of tetrahedral cells until we have obtained an accurate description of the boundary layer with a given mesh resolution. This task should be automatically addressed when one has to adapt the mesh frequently to contain the solution progression within refined regions. Our method was based on coarsening or refinement techniques to reduce interpolation error without node displacement. However, there is a window opportunity to construct meshes using an unsteady mesh adaptation algorithm. In this case, we have to base local or globally the gradation of tetrahedral meshes and simultaneously estimate the error from the conversion profile addressing every time step computed by the multiphase flow VOF solver.

Nevertheless, following the successive mesh improvements already reported in previous works when the computational grid was refined to give 3×10^6 of tetrahedral cells, the same performance was repeated as to 2.6×10^6 cells confirming that the solutions obtained with the higher densities were already converged. This methodology avoided the application complexity of mesh adaptation algorithms; however, to control the accuracy of the solutions produced by successive refinements, we have also optimized the time step to provide realistic three-dimensional simulations of the catalytic wet oxidation under PFCs as will be discussed later. In

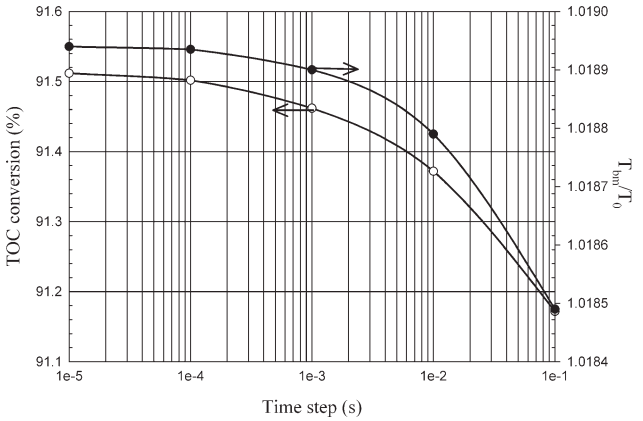

Figure 2. Effect of time step on Total Organic Carbon conversion and normalized bulk temperature.

$T = 200$ °C, $G = 0.5$ kg/m^{2}s, $P = 30$ bar, ON–OFF liquid flow modulation: $L = 9$ kg/m^{2}s $\rightarrow L = 3$ kg/m^{2}s $\rightarrow L = 9$ kg/m^{2}s.

addition to the concentration profile, several computational runs were performed changing the number of computational nodes in the above-mentioned range to evaluate quantitatively the temperature profile. Figure 1 also shows the effect of mesh density on this variable when the catalytic wet oxidation was simulated at $G = 0.5$ kg/m^{2}s, $T = 200$°C, and $P = 30$ bar following the similar ON–OFF liquid flow modulation ($L = 9$ kg/m^{2}s $\rightarrow L = 3$ kg/m^{2}s $\rightarrow L = 9$ kg/m^{2}s). Once more, as soon as we used a computational grid comprising 2.6 million of tetrahedral cells the VOF model predictions converged and the monotony of concentration and temperature profiles exhibited by Figure 1 was comparable.

As with different mesh densities, the time-stepping scheme used for the temporal discretization of the constitutive equations affects significantly the accuracy of the CFD simulations, so here we evaluated first-order and second-order time discretization methods. The later one was selected due to high inherent accuracy entailing different values for the time step in the range: 10^{-5}, 10^{-4}, 10^{-3}, and 10^{-2} s. The time step sensitivity tests are portrayed in Figure 2 for the conversion and temperature profiles at $G = .5$ kg/m^{2}s, $T = 200$°C, and $P = 30$ bar following the ON–OFF liquid flow modulation ($L = 9$ kg/m^{2}s $\rightarrow L = 3$ kg/m^{2}s $\rightarrow L = 9$ kg/m^{2}s). A different asymptotic behavior was observed in the concentration and temperature profiles as functions of time step in comparison to the plots depicted by Figure 1. Although the highest number of computational nodes gave the better predictions either for the concentration or the temperature, the same performance was now attained with the lowest valued time step. It should be also referred that those profiles exhibited similar behaviors in what respect to the uniformity of increasing and decreasing order of the time step plots for the total organic carbon conversion and temperature computations, respectively. This fact is mainly connected with the thermodynamic (exothermic) and kinetic (Arrhenius's law) considerations encompassed by the liquid-phase oxidation of phenol-like pollutants.

Influence of oxidation temperature

The oxidation temperature plays a major role amongst other operating parameters for the catalytic detoxification of liquid pollutants. Figure 3 shows the axial profile of normalized concentration results at $T = 160$°C, $G = 0.5$ kg/m^{2}s, and $P = 30$ bar following the ON–OFF liquid flow modulation ($L = 9$ kg/m^{2}s $\rightarrow L = 3$ kg/m^{2}s $\rightarrow L = 9$ kg/m^{2}s). As can be seen, in the first half of the TBR, the conversion profile computed by the CFD model for PFCs represented by the solid line was roughly similar to the one calculated for the trickling flow regime (TFC). However, the normalized concentration for the PFC was substantially lower than for the TFC, which means that the total organic carbon conversions attained for the PFC were higher than for the TFC at the reactor outlet. At the reactor outlet, the experimental conversion was 79.0%, and this value has a closer proximity to the computed PFC value, 83.1%, in comparison with the predicted conversion value obtained for the TFC simulation, 73.8%, see Figure 3. It should be noted that the total organic carbon conversion for the PFC was computed following the ON–OFF liquid modulation that is characterized by base and peak times, base and peak velocities, split ratio, and also by a barycentric velocity in opposition to the constant throughput mode, henceforth labeled also as isoflow mode (TFC). In fact, if one compares the experimental conversion data obtained at $z = 20$, 40, 60, 80, and 100 cm that were 29.9, 50.3, 57.2, 77.3, and 81.4%, respectively, we found a good agreement between these data and the computed conversion values at the same axial locations: for $z = 20$, 40, 60, 80, and 100 cm the VOF model predicted 33.3, 52.6, 59.5, 78.9, and 83.1%, respectively. Therefore, it is worth remarking the confidence exhibited by the CFD simulations, which underline the PFC mode as one promising regime to improve the environmental performance of trickle beds, especially when the mass transfer of a key reactant is rate controlling or, at least, affects the mineralization rate.

Particularly, the liquid flow modulation that was achieved by pulsing directly the liquid loading, that is, switching the liquid flow rate between a minimum ($L = 3$ kg/m^{2}s) and a

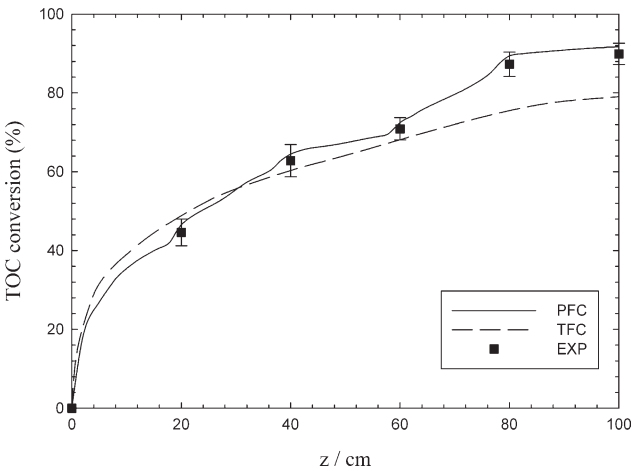

Figure 3. Axial profile of the computed and experimental results for the TOC conversion.

$T = 160$ °C, $G = 0.5$ kg/m^{2}s, $P = 30$ bar, ON–OFF liquid flow modulation: $L = 9$ kg/m^{2}s $\rightarrow L = 3$ kg/m^{2}s $\rightarrow L = 9$ kg/m^{2}s.

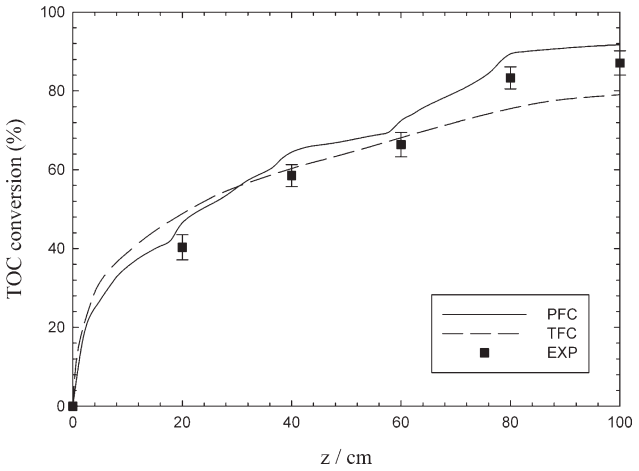

Figure 4. Axial profile of the computed and experimental results for the TOC conversion.

$T = 200$ °C, $G = 0.5$ kg/m^{2}s, $P = 30$ bar, ON–OFF liquid flow modulation: $L = 9$ kg/m^{2}s $\rightarrow L = 3$ kg/m^{2}s $\rightarrow L = 9$ kg/m^{2}s.

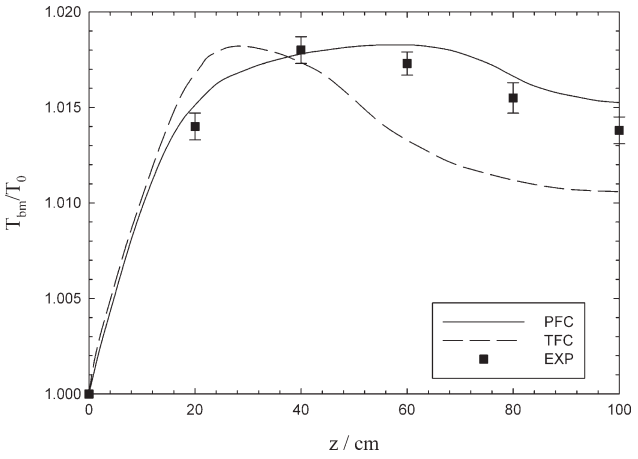

Figure 5. Axial profile of the computed and experimental results for the normalized temperature.

$T = 160$°C, $G = 0.5$ kg/m^{2}s, $P = 30$ bar, ON–OFF liquid flow modulation: $L = 9$ kg/m^{2}s $\rightarrow L = 3$ kg/m^{2}s $\rightarrow L = 9$ kg/m^{2}s.

maximum value ($L = 9$ kg/m^{2}s) has been found to advance the oxidation of phenol-like compounds. The operational advantage entailed by this process intensification can be sustained by the fact that the trickle bed reaction system is governed by the gas oxidant. As reported in the literature for gas phase limited reactions,[23] the oxygen acts as an adverse reactant because of its limiting accessibility via internal and/or external mass transport. Mainly because liquid streams are reshuffled and shredded by the packed bed layers being subsequently reassembled, the catalytic packing acts as internal distributors repairing with higher or lesser extension the gas liquid distribution, whereas fluids progress downward. In this regard, the liquid flow modulation is speculated to confer more exposure of the catalyst surface to oxygen, thereby promoting the mineralization efficiency. Moreover, this operation led to improved conversions and exerted a positive effect on the reaction selectivity toward carbon dioxide production and concomitantly enhancing the oxidation of partially oxidized intermediate compounds.

The axial profile of the total organic carbon conversion at $T = 200$°C, $G = 0.5$ kg/m^{2}s, and $P = 30$ bar following the ON–OFF liquid flow modulation ($L = 9$ kg/m^{2}s $\rightarrow L = 3$ kg/m^{2}s $\rightarrow L = 9$ kg/m^{2}s) is portrayed by Figure 4. As can be seen from the comparison between Figures 3 and 4, whereas the conversion PFC profile surpassed the TFC one in the second half of the TBR at the lowest temperature ($T = 160$°C), this was not the case at the highest temperature ($T = 200$°C). The increase of oxidation temperature was found to move the transcendent point on the total organic carbon concentration toward the top of the trickle bed. In fact, the experimental data obtained for $z = 20$, 40, 60, 80, and 100 cm were 42.7, 60.8, 68.7, 85.7, and 89.5%, whereas the computed conversions were 46.3, 64.3, 72.3, 89.1, and 91.5%, respectively. At the highest temperature, the total organic carbon conversion attained under trickling flow conditions at the reactor outlet was 78.9%, so this was the operating temperature that gave the higher discrepancies between the PFC and TFC operation modes.

Figure 5 shows the axial profile of normalized temperature at $T = 160$°C, $G = 0.5$ kg/m^{2}s, and $P = 30$ bar following the ON–OFF liquid flow modulation ($L = 9$ kg/m^{2}s $\rightarrow L = 3$ kg/m^{2}s $\rightarrow L = 9$ kg/m^{2}s), whereas Figure 6 depicts the computed thermal profile when increasing the oxidation temperature up to $T = 200$°C keeping everything else. As can be seen from both Figures 5 and 6, the PFCs encompassed by the aforementioned ON–OFF liquid flow modulation scheme have been found to be responsible to move the maximum bulk temperature increase toward the reactor outlet in comparison with the TFC mode of operation. The experimental temperature data obtained for $z = 20$, 40, 60, 80, and 100 cm were 1.51, 1.78, 1.83, 1.66, and 1.53% at the lowest temperature, and it increased slightly to 1.79, 2.06, 2.11,

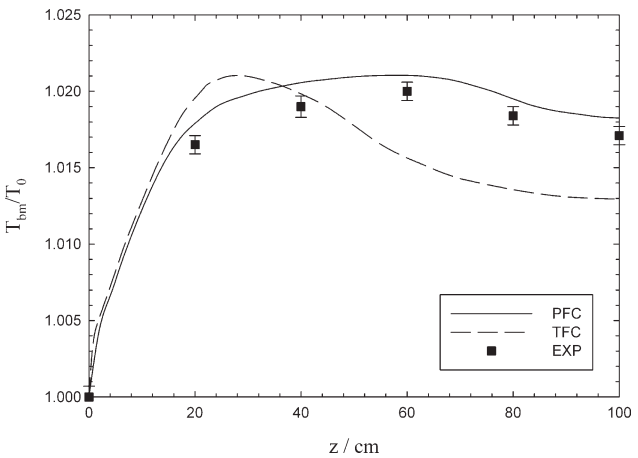

Figure 6. Axial profile of the computed and experimental results for the normalized temperature.

$T = 200$°C, $G = 0.5$ kg/m^{2}s, $P = 30$ bar, ON–OFF liquid flow modulation: $L = 9$ kg/m^{2}s $\rightarrow L = 3$ kg/m^{2}s $\rightarrow L = 9$ kg/m^{2}s.

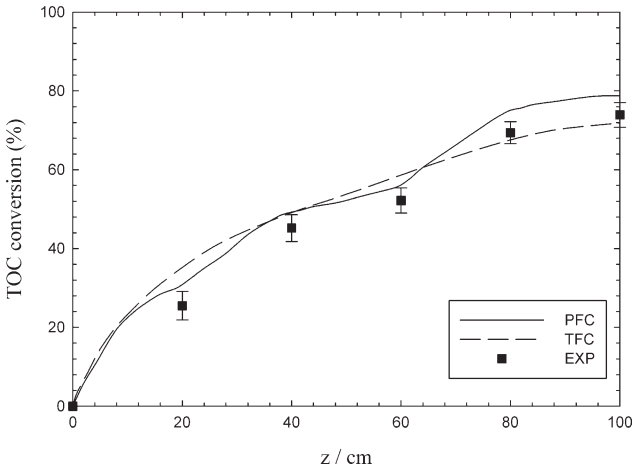

Figure 7. Axial profile of the computed and experimental results for the TOC conversion.

$T = 160$°C, $G = 0.7$ kg/m^{2}s, $P = 30$ bar, ON–OFF liquid flow modulation: $L = 9$ kg/m^{2}s $\rightarrow L = 3$ kg/m^{2}s $\rightarrow L = 9$ kg/m^{2}s.

1.95, and 1.82% increasing the temperature to $T = 200$°C, respectively. Indeed, the better agreement between computed results and experimental data was observed for the highest temperature. The maximum bulk temperature increase was achieved at $z = 59$ cm with an intensity of 1.84% for $T = 160$°C, whereas this value shifted to 2.12% at $z = 55$ cm for $T = 200$°C, which reinforces once again the effect of temperature under PFCs. This fact can be additionally supported by the intersection points between the PFC and TFC temperature profiles illustrated by Figures 7 and 8, so they were located at $z = 41$ and 32 cm for $T = 160$ and 200°C, respectively.

Effect of liquid flow rate

Provided that liquid flow rate plays a considerable outcome on the reaction yield, process parameters including the velocity at which the pulse front travels along the bed, the frequency of pulsations, and the structure of pulses being formed or the size of the liquid-rich and gas-rich zones have been investigated comparatively to agitated vessels on the hydrogenation of poly(styrene) over a Pd/Al_2O_3 catalyst.[24] As three-phase reactors can suffer from rivulet formation and inhomogeneous residence time distributions in such cumbersome systems, here we also evaluate the influence of the liquid flow rate. The VOF model predictions of the normalized concentration profile following the ON–OFF liquid flow modulation ($L = 9$ kg/m^{2}s $\rightarrow L = 3$ kg/m^{2}s $\rightarrow L = 9$ kg/m^{2}s) can then be further corroborated with the hydrodynamic assertions realized for pulsing flows in trickle beds. To accomplish such a task, one should be aware that liquid pulsations generated via ON–OFF liquid, ON–OFF gas, and gas/liquid alternating cyclic operations should not be bewildered with the liquid pulses that are initiated in pulse flow regime due to the high interaction between liquid and gas phases.

The analysis of the ON–OFF liquid flow modulations portrayed by Figures 3 and 4 indicates that the frequency of the traveling liquid pulsations is responsible by the shape of the axial concentration profile. The propagation along the bed main axis of the imposed liquid pulsations is the consequence of preimposed liquid holdup time series at different bed positions. We have followed the variation of the total organic carbon concentration as it facilitates the validation of the VOF model at as many as desired vertical positions. Particular attention was paid to the experimental runs to avoid any superfluous experimental biases that may arise due to local external wall sampling irregularities. During the course of ON–OFF liquid cyclic operations, the concentration data profile was attenuated when liquid pulsations were carried out at the lower liquid flow rates. At $L = 3$ kg/m^{2}s, the normalized concentration series close to the top of the TBR exhibited sharp fronts and gradually become less intense as they travel downward. The nonisolated nature of the traveling liquid pulsations results from axial dispersion. As the liquid pulsations decay along the catalyst bed, a considerable fraction of the liquid content is left behind. Indeed, a similar phenomenon occurs temporally, with almost stagnant liquid pockets remaining in the bed as it undergoes peak to base cyclic operations. This phenomenon helps maintain a relatively even multiphase flow distribution, which was also promoted by operating in fast pulsing mode at 0.05 Hz. Operation in this manner prevents the total collapse of liquid pulses that could lead to a dry bed during the OFF cycle.

Effect of gas flow rate

Being aware that liquid pulsations are also affected by the gas flow rate, we have also performed additional simulations to evaluate on how the ON–OFF liquid flow modulations can be compared with ON–OFF gas and gas/liquid alternating strategies. Having examined that the pulsations near the bed entrance experience some degree of attenuation, they nonetheless were able to conserve a regular morphology at the approach of the reactor outlet. This behavior underlined

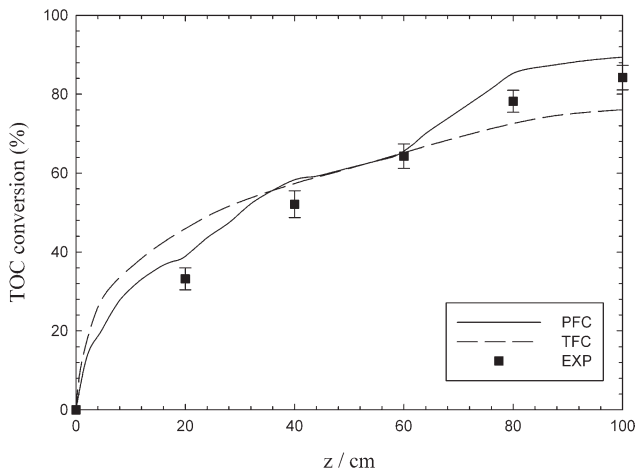

Figure 8. Axial profile of the computed and experimental results for the TOC conversion.

$T = 200$°C, $G = 0.7$ kg/m^{2}s, $P = 30$ bar, ON–OFF liquid flow modulation: $L = 9$ kg/m^{2}s $\rightarrow L = 3$ kg/m^{2}s $\rightarrow L = 9$ kg/m^{2}s.

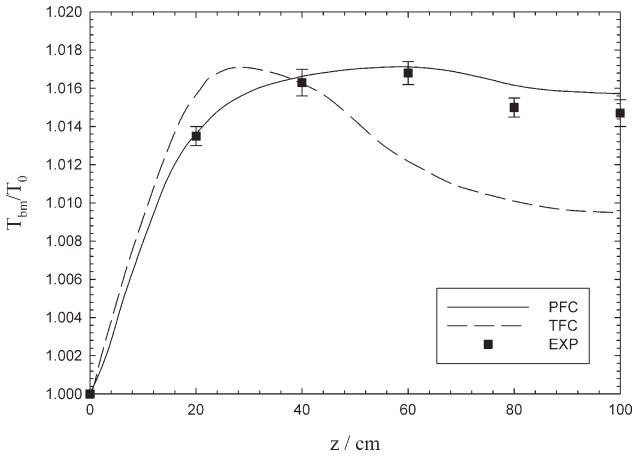

Figure 9. Axial profile of the computed and experimental results for the normalized temperature.

$T = 160°C$, $G = 0.7$ kg/m^{2}s, $P = 30$ bar, ON–OFF liquid flow modulation: $L = 9$ kg/m^{2}s $\rightarrow L = 3$ kg/m^{2}s $\rightarrow L = 9$ kg/m^{2}s.

the significant role of gas phase flow, so it acts as a kind of isolating agent to keep distinct liquid slugs. This latter feature can in all likelihood be intensified as the resumptions of the gas flow are used to eliminate or at least minimize the leakage of the liquid payloads from the moving liquid pulsations, thereby safeguarding the wavy nature of liquid flow. Despite intrinsic advantages of ON–OFF gas and gas/liquid alternating cyclic operations, the influence of gas flow rate was mostly investigated through the computed results illustrated by Figure 7.

To distinguish the evolving patterns of the axial total organic carbon concentration under different gas flow rates, Figure 7 shows the total organic carbon conversion profile increasing the gas flow rate to $G = 0.7$ kg/m^2 at the lowest temperature, $T = 160°C$, and $P = 30$ bar following the ON–OFF liquid flow modulation ($L = 9$ kg/m^{2}s $\rightarrow L = 3$ kg/m^{2}s $\rightarrow L = 9$ kg/m^{2}s). As can be seen in Figure 7, the experimental data obtained for $z = 20$, 40, 60, 80, and 100 cm were 27.8, 47.6, 54.5, 71.8, and 76.3%, whereas the VOF model predictions were 30.9, 49.4, 56.1, 75.1, and 78.9%, respectively. These computed results unveiled lower total organic carbon conversions in comparison with the ones attained at $G = 0.5$ kg/m^2, $T = 160°C$, and $P = 30$ bar. In fact, at the lowest gas flow rate the conversion data obtained at $z = 20$, 40, 60, 80, and 100 cm were 29.9, 50.3, 57.2, 77.3, and 81.4%, whereas the computed concentration values at the same axial locations were 33.3, 52.6, 59.5, 78.9, and 83.1%, respectively, see Figure 3. At this point, it would be meaningful to mention how we investigated the effect of gas flow rate. For the sake of clarity, we have charged the gas flow rate in the range 0.1–0.9 kg/m^{2}s with gradual 0.1 kg/m^{2}s steps. We found that within this assortment of operating conditions, the optimum gas flow rate was located between 0.5 and 0.7 kg/m^{2}s, and so, we have concentrated the remainder of the discussion on the above-mentioned oxidation conditions.

Figure 8 shows the VOF simulations of the normalized total organic carbon conversion profile at $T = 200°C$ while maintaining the same gas flow rate and operating pressure. The computed axial concentration results obtained for $z = 20$, 40, 60, 80, and 100 cm were 35.6, 54.5, 66.7, 80.6, and 86.7% respectively. From the comparison between Figures 6 and 8, the conversion decreased when increasing the gas flow rate and the axial position of the intersection point between the PFC and TFC profiles was pushed down the TBR. Indeed, for a constant gas and liquid velocity, the liquid flow modulations present similar liquid holdup values to the trickling flow conditions. As observed experimentally, the gas cyclic operations exhibited a decreasing trend on the liquid volumetric fraction as well as on the total organic carbon concentration. A palpable explanation for this observation is related to the higher gas superficial velocities; so, the gas phase has a more prominent effect on the agglomeration of liquid within the catalytic bed, which produced most likely lesser liquid holdup. The higher gas superficial velocities were ascribed to result in lower liquid holdup as one would expect under steady-state operation.

The axial profiles of the normalized bulk temperature are shown in Figure 9 at $G = 0.7$ kg/m^{2}s, $T = 160°C$, and $P = 30$ bar following the ON–OFF liquid flow modulation ($L = 9$ kg/m^{2}s $\rightarrow L = 3$ kg/m^{2}s $\rightarrow L = 9$ kg/m^{2}s), whereas Figure 10 depicts the computed thermal profile when increasing the oxidation temperature up to $T = 200°C$ at the same gas and liquid flow rates. The catalytic wet oxidation for such operating conditions during the ON–OFF liquid cyclic operations has experienced somehow a shrinking effect on the axial temperature profile. Specifically, the experimental temperature data obtained for $z = 20$, 40, 60, 80, and 100 cm were 1.05, 1.33, 1.38, 1.20, and 1.17% at the lowest temperature (Figure 9), and it increased slightly to increasing the temperature to $T = 200°C$ (Figure 10), respectively. At $T = 160°C$, the VOF model predictions at $z = 20$, 40, 60, 80, and 100 cm were 1.36, 1.66, 1.71, 1.62, and 1.57%, whereas the computed results at the highest temperature agreed better with the experimental data leading to the axial normalized

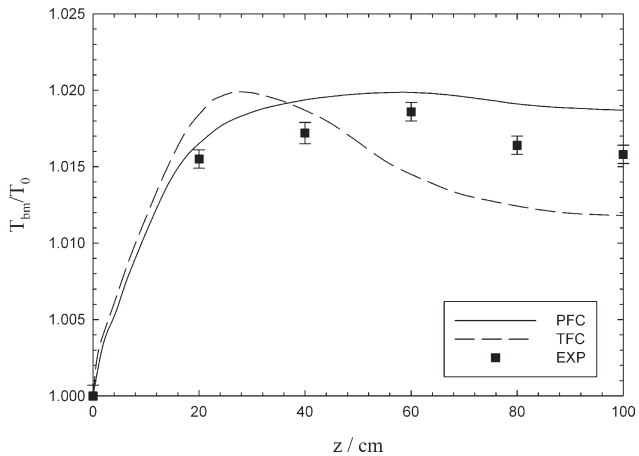

Figure 10. Axial profile of the computed and experimental results for the normalized temperature.

$T = 200°C$, $G = 0.7$ kg/m^{2}s, $P = 30$ bar, ON–OFF liquid flow modulation: $L = 9$ kg/m^{2}s $\rightarrow L = 3$ kg/m^{2}s $\rightarrow L = 9$ kg/m^{2}s.

temperature profile: 1.65, 1.94, 1.99, 1.91, and 1.87%. As mentioned before, the liquid pulsations are gradually faded away while traveling downstream. This effect can be even aggravated depending on the cycle frequency used to modulate the gas–liquid flow. Such a methodology was found to promote the detoxification of organic matter highlighting the benefits of process intensification covered by the computed and experimental PFC results in comparison with the TFC ones.

VOF mappings of liquid pulsations

The morphological features of the interstitial flow under forced liquid pulsations have been analyzed according to the computational maps of the liquid phase distribution. On the CFD simulations performed at $G = 0.5$ kg/m^2, $T = 200$°C, and $P = 30$ bar following the ON–OFF liquid flow modulation ($L = 9$ kg/m^{2}s $\rightarrow L = 3$ kg/m^{2}s $\rightarrow L = 9$ kg/m^{2}s), Figure 11 shows an instantaneous snapshot of liquid-phase distribution colored by total organic carbon concentration, whereas the temperature distribution is portrayed in Figure 12 at the same operating conditions. As mentioned before for the computed-normalized concentration results, the liquid pulsations underwent considerable attenuation as they move along the catalytic bed. The three-dimensional diagrammatic representations have shown sizable loads of liquid accumulations. This fact arose mainly due to the burst of liquid and gas slices attained under forced operation that were initiated periodically at the reactor inlet. As time progresses, the liquid payloads are weakened by the dissipation effect exerted by the solid packing. The liquid pulsations were then stabilized thereby safeguarding a fraction of the original amplitude imposed at the top of the TBR. If one increases the gas flow rate to $G = 0.5$ kg/m^{2}s, the liquid holdup is decreased, and higher conversions of organic matter are achieved. However, if one increases even further to $G = 0.7$ kg/m^{2}s, the multiphase reacting system reaches the maximum allowable gas flow rate to produce better decontamination rates, which means that we have previously achieved an optimum for the detoxification reaction by catalytic wet air oxidation. Concomitantly, as the gas–liquid interactions increased by such a mechanism, the oscillations of liquid volumetric fraction that are typically encountered under trickle flows are leveled off further within the trickle bed, which can be used to improve substantially the multiphase flow distribution at peak circumstances.

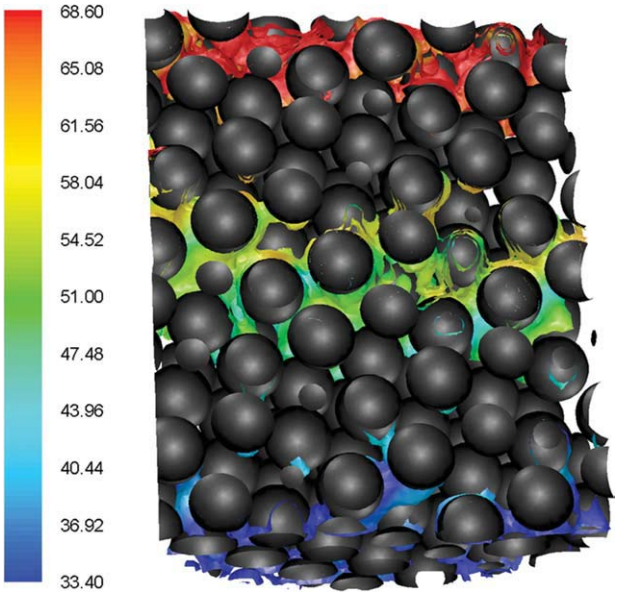

Figure 11. Instantaneous snapshot of liquid phase distribution colored by total organic carbon concentration.

$T = 200$°C, $G = 0.5$ kg/m^{2}s, $P = 30$ bar, ON–OFF liquid flow modulation: $L = 9$ kg/m^{2}s $\rightarrow L = 3$ kg/m^{2s} $\rightarrow L = 9$ kg/m^{2}s. [Color figure can be viewed in the online issue, which is available at wileyonlinelibrary.com.]

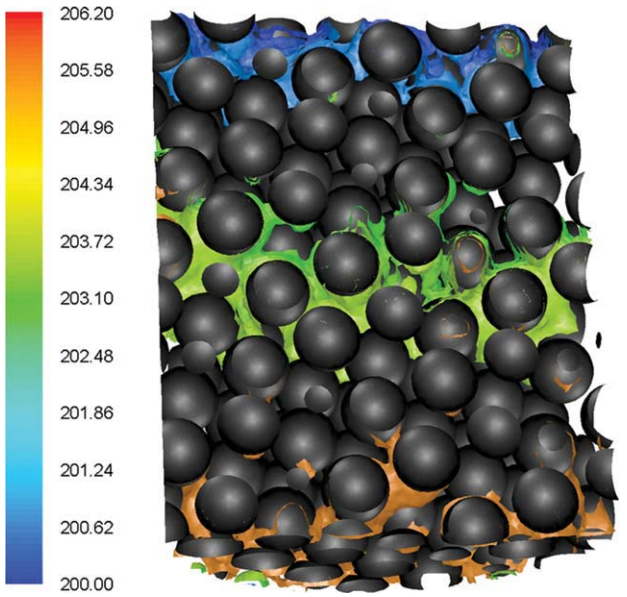

Figure 12. Instantaneous snapshot of liquid phase distribution colored by liquid temperature.

$T = 200$°C, $G = 0.5$ kg/m^{2}s, $P = 30$ bar, ON–OFF liquid flow modulation: $L = 9$ kg/m^{2}s $\rightarrow L = 3$ kg/m^{2}s $\rightarrow L = 9$ kg/m^{2}s. [Color figure can be viewed in the online issue, which is available at wileyonlinelibrary.com.]

During the liquid cyclic operations portrayed by Figures 11 and 12 for the computed concentration and temperature maps, the gas flow rate was permanently fixed across the bed. As one expected, the gas flow was persistent near the wall of TBR as this zone included larger bed porosities. The liquid phase competed with the gas phase within the interstitial space, which forced the incoming liquid to be routed across the least resistance zones of the bulk space. This latter feature can be magnified when the amount of liquid held in high interaction zones exceeds the maximum allowed liquid payload conveyable under trickle flow regime. Guided by this provision, the liquid flows corewise in the trickle bed exhibiting a regular and periodic shape. The overall action results in a superior averaged gas–liquid distribution being the excess liquid transported via the pulse formation. Therefore, the total organic carbon conversions are intensified allowing us to obtain higher mineralization efficiencies.

Conclusions

Pulsing flow in TBRs has been claimed to promote the averaged heat and mass transfer rates, thereby enhancing the overall conversion and productivity. In this work, we focused on the mineralization of organic matter by catalytic wet oxidation at different liquid flow modulations. The convective nature of the disturbances that lead to pulsing was simulated by a VOF CFD model and validated with experimental data. To evaluate the predicted effects of pulsing on reaction outcome, the multiphase flow governing equations were detailed with the computational methodology used in the simulation procedure. Prominent numerical parameters were optimized in terms of mesh aperture and time step. Several computational runs were performed addressing the effect of nominal gas and liquid flow rates as well as the oxidation temperature. Here, we found that the concentration profile computed by the CFD model for PFCs demonstrated superior oxidation performance over the trickling flow regime, which has been further corroborated by experimental evidences. Afterward, the normalized concentration series close to the top of the TBR exhibited sharp fronts and gradually become less intense as they travel downward that reflected the nonisolated nature of the traveling liquid pulsations. Finally, these computational and experimental findings enabled us to intensify the detoxification of high-strength wastewaters and can be further exploited due to advantageous dispersive and convective heat/mass transfer phenomena under PFCs.

Notation

C_μ, $C_{1\varepsilon}$, $C_{2\varepsilon}$ = k–ε model parameters: 0.09, 1.44, 1.92
C = specific concentration (ppm)
c_p = specific heat (J/(kg K))
D = mass diffusivity (m^2 s^{-1})
d_p = catalyst particle nominal diameter (m)
E = thermal energy (J)
$\vec{g}$ = gravitational acceleration (9.81 m/s^2)
G = gas mass flux (kg/m^2s)
G_{kL} = generation rate of turbulent kinetic energy
h = convective heat transfer coefficient (W/(m^2K))
$\mathbf{I}_q$ = interphase momentum exchange term
k = k–ε model kinetic energy
K = mass transfer coefficient (m s^{-1})
k_f = thermal conductivity (W/(m K))
k_{eff} = effective thermal conductivity (W/(m K))
l = characteristic length (m)
L = liquid mass flux (kg/m^2s)
$\hat{n}_w$ = unit vector normal to the wall
Nu = nusselt number [hl/k_f], dimensionless
p = pressure (bar)
Pr = Prandtl number [$C_p\mu/k_f$], dimensionless
$-r$ = oxidation rate ((mg/L) × (1/min))
Re_q = Reynolds number of qth phase [$(\rho_q u_q d_p/\mu_q$], dimensionless
S_i = source mass for phase i (ppm)
Sh = Sherwood number [Kl/D], dimensionless
S_h = source term containing volumetric reaction heat (J)
t = time (s)
$\hat{t}_w$ = unit vector tangential to the wall
T = temperature (K)
TOC = total organic carbon (ppm)
$\vec{u}$ = superficial vector velocity (m/s)
z = axial coordinate (m)

Greek letters

α_i = volume fraction of ith phase
ε = k-ε model dissipation energy
κ = gas–liquid interface curvature
ρ_q = density of qth phase (kg/m^3)
Δp = total pressure drop (Pa)
σ = surface tension coefficient
σ_k , σ_ε = k-ε model parameters: 1.2, 1.0
τ = residence time (s)
$\overline{\overline{\tau_q}}$ = viscous stress tensor of qth phase (Pa)
$\overline{\overline{\tau_{t,q}}}$ = turbulent stress tensor of qth phase (Pa)
θ_w = contact angle at the wall
μ_q = viscosity of qth phase (Pa s)

Subscripts

G = gas phase
q = qth phase
L = liquid phase
S = solid phase

Acknowledgments

The authors gratefully acknowledged the financial support of Fundação para a Ciência e Tecnologia, Portugal.

Literature Cited

1. Dudukovic MP, Larachi F, Mills PL. Multiphase reactors—revisited. *Chem Eng Sci*. 1999;54:1975–1995.
2. Bhargava SK, Tardio J, Prasad J, Foger K, Akolekar DB, Grocott SC. Wet oxidation and catalytic wet oxidation. *Ind Eng Chem Res*. 2006;45:1221–1258.
3. Ayude A, Rodriguez T, Font J, Fortuny A, Bengoa C, Fabregat A, Stüber F. Effect of gas feed flow and gas composition modulation on activated carbon performance in phenol wet air oxidation. *Chem Eng Sci*. 2007;62:7351–7358.
4. Guo J, Al-Dahhan M. Catalytic wet air oxidation of phenol in concurrent downflow and upflow packed-bed reactors over pillared clay catalyst. *Chem Eng Sci*. 2005;60:735–746.
5. Sundaresan S. Mathematical modeling of pulsing flow in large trickle beds. *AIChE J*. 1987;33:455–469.
6. Grosser K, Carbonell RG, Sundaresan S. Onset of pulsing in two-phase cocurrent downflow through a packed bed. *AIChE J*. 1988;34:1850–1860.
7. Dankworth DC, Kevrekidis IG, Sundaresan S. Dynamics of pulsing flow in trickle beds. *AIChE J*. 1990;36:605–621.
8. Wilhite BA, Wu R, Huang X, McCready MJ, Varma A. Enhancing performance of three-phase catalytic packed-bed reactors. *AIChE J*. 2001;47:2548–2556.
9. Anadon LD, Sederman AJ, Gladden LF. Mechanism of the trickle-to-pulse flow transition in fixed-bed reactors. *AIChE J*. 2006;52:1522–1532.
10. Attou A, Ferschneider GA. Two-fluid model for flow regime transition in gas–liquid trickle-bed reactors. *Chem Eng Sci*. 1999;54:5031–5037.
11. Jiang Y, Khadilkar MR, Al-Dahhan MH, Dudukovic MP. CFD modeling of multiphase in packed bed reactors: results and applications. *AIChE J*. 2002;48:716–730.
12. Iliuta I, Larachi F, Al-Dahhan MH. Double-slit model for partially wetted trickle flow hydrodynamics. *AIChE J*. 2000;46:597–609.
13. Souadnia A, Latifi MA. Analysis of two-phase flow distribution in trickle-bed reactors. *Chem Eng Sci*. 2001;56:5977–5985.
14. Gunjal PR, Kashid MN, Ranade VV, Chaudhari RV. Hydrodynamics of trickle-bed reactors: experiments and CFD modeling. *Ind Eng Chem Res*. 2005;44:6278–6294.
15. Lopes RJG, Quinta-Ferreira RM. Numerical simulation of trickle-bed reactor hydrodynamics with RANS-based models using a volume-of-fluid technique. *Ind Eng Chem Res*. 2009;48:1740–1748.
16. Brackbill J, Kothe D, Zemach C. A continuum method for modelling surface tension. *J Comput Phys*. 1992;100:335–354.
17. Lopes RJG, Quinta-Ferreira RM. Volume-of-fluid-based model for multiphase flow in high-pressure trickle-bed reactor: optimization of numerical parameters. *AIChE J*. 2009;55:2920–2933.
18. Massa P, Ayude MA, Ivorra F, Fenoglio R, Haure P. Phenol oxidation in a periodically operated trickle bed reactor. *Catal Today*. 2005;107–108:630–636.

19. Satterfield CN, van Eek MW, Bliss GS. Liquid-solid mass transfer in packed beds with downward concurrent gas-liquid flow. *AIChE J*. 1978;24:709–717.
20. Boelhouwer JG, Piepers HW, Drinkenburg AAH. Particle-liquid heat transfer in trickle-bed reactors. *Chem Eng Sci*. 2001;56: 1181–1187.
21. Lopes RJG, Silva AMT, Quinta-Ferreira RM. Screening of catalysts and effect of temperature for kinetic degradation studies of aromatic compounds during wet oxidation. *Appl Catal B*. 2007;73: 193–202.
22. Lopes RJG, Quinta-Ferreira RM. Assessment of CFD Euler–Euler method for trickle-bed reactor modelling in the catalytic wet oxidation of phenolic wastewaters. *Chem Eng J*. 2010;160:293–301.
23. Al-Dahhan MH, Larachi F, Dudukovic MP, Laurent A. High pressure trickle-bed reactors: a review. *Ind Eng Chem Res*. 1997;36:3292–3314.
24. Bussard A, Dooley KM. Polymer hydrogenation in pulsed flow systems with extrusion. *AIChE J*. 2008;54:1064–1072.

Manuscript received Oct. 12, 2010, and revision received Jan. 27, 2011.